

ARTICLE OPEN



Tailoring exciton dynamics in TMDC heterobilayers in the ultranarrow gap-plasmon regime

Mahfujur Rahaman¹, Gwangwoo Kim^{1,2}, Kyung Yeol Ma³, Seunguk Song¹, Hyeon Suk Shin³ and Deep Jariwala¹✉

Control of excitons in transition metal dichalcogenides (TMDCs) and their heterostructures is fundamentally interesting for tailoring light-matter interactions and exploring their potential applications in high-efficiency optoelectronic and nonlinear photonic devices. While both intra- and interlayer excitons in TMDCs have been heavily studied, their behavior in the quantum tunneling regime, in which the TMDC or its heterostructure is optically excited and concurrently serves as a tunnel junction barrier, remains unexplored. Here, using the degree of freedom of a metallic probe in an atomic force microscope, we investigated both intralayer and interlayer excitons dynamics in TMDC heterobilayers via locally controlled junction current in a finely tuned sub-nanometer tip-sample cavity. Our tip-enhanced photoluminescence measurements reveal a significantly different exciton-quantum plasmon coupling for intralayer and interlayer excitons due to different orientation of the dipoles of the respective e - h pairs. Using a steady-state rate equation fit, we extracted field gradients, radiative and nonradiative relaxation rates for excitons in the quantum tunneling regime with and without junction current. Our results show that tip-induced radiative (nonradiative) relaxation of intralayer (interlayer) excitons becomes dominant in the quantum tunneling regime due to the Purcell effect. These findings have important implications for near-field probing of excitonic materials in the strong-coupling regime.

npj 2D Materials and Applications (2023)7:66; <https://doi.org/10.1038/s41699-023-00428-7>

INTRODUCTION

Coulomb-bound electron-hole (e - h) pairs, commonly known as excitons, govern the optical properties of monolayer transition metal dichalcogenides (TMDCs) due to their large binding energies (on the scale of 0.5 eV) and oscillator strengths¹. As a result, the fundamental optical properties of these materials are dominated by many body excitonic resonances, even at room temperature (RT). Furthermore, in a homo/hetero-bilayer (HBs) sample made from TMDCs, ultrafast interlayer charge transfer can also facilitate the formation of interlayer excitons (ILXs) with long lifetimes and large exciton binding energies observed at RT in prior work². Therefore, TMDCs have attracted significant attention for both fundamental studies of novel quantum optical phenomena and photonic/optoelectronic applications in recent times^{3–9}.

TMDCs possess strong light-matter coupling at excitonic resonances in the visible part of the spectrum, with almost ideal two-dimensional (2D) confinement, making it easier to control the excitonic parameters, such as resonance energies, oscillator strength, radiative and nonradiative lifetimes on demand^{10–14}. Therefore, one way of controlling excitons is to manipulate them via plasmonic coupling, using plasmonic resonances in noble metal nanostructures, which are also in the visible spectrum. In particular, the use of metallic nanostructures in the proximity of TMDC monolayers can create both weak and strong coupling regimes for excitons, and thus, control the emission energies, decay rates, radiative, and nonradiative lifetimes^{15–17}.

In general, excitons in TMDCs in proximity to a plasmonic system can be treated as dipole emitters, whose emission can be expanded into multipoles centered around the plasmonic energy¹⁸. Hence, the strength of coupling between the exciton and plasmon, and the associated manipulation of excitonic parameters, depends on the individual field polarizability.

Therefore, the manipulation of intralayer (in-plane polarization) and interlayer (out-of-plane polarization) excitonic parameters in TMDC HBs via a plasmonic cavity can be different due to their different polarization states. ILXs, in particular, show great tunability in a plasmonic cavity as a function of cavity size in the z -direction (i.e., coupling efficiently to the ILX polarization), resulting in the amplification of both exciton decay rate and radiative lifetime^{19,20}. However, as the cavity size is further tuned from nanometer to sub-nm gap (in the quantum plasmonic regime), a strong interaction between the plasmonic field and ILX results in more nonradiative loss. Whereas in-plane polarized intralayer excitons show an opposite trend as the size of the cavity decreases further in the sub-nm scale due to the Purcell effect²¹.

The ultrafast exciton-plasmon interaction dynamics are generally probed via pump-probe and time-resolved PL measurements in a conventional optical configuration in the form of overall PL lifetimes of the excitonic species^{22,23}. However, it is not feasible to finely control cavity size in the sub-nm scale and simultaneously probe the exciton-plasmon interaction dynamics, let alone discern radiative and nonradiative contributions using a conventional setup. Recently, a qualitative approach of determining the individual contribution of radiative and nonradiative decays and the Purcell effect on intralayer and interlayer excitons in TMDC HBs has been proposed using tip-enhanced photoluminescence (TEPL) configuration in a finely tuned sub-nm cavity²¹. In this approach, the PL measured from both intralayer and interlayer excitonic emissions in a sub-nm cavity can be fitted using a rate equation model to discern the contribution of Purcell enhancing/quenching, radiative, and nonradiative lifetimes. Although the model, effectively deconvoluted all the contributing parameters, an important question remained unanswered, which is how these parameters evolved in a quantum plasmonic regime

¹Department of Electrical and Systems Engineering, University of Pennsylvania, Philadelphia, PA 19104, USA. ²Department of Engineering Chemistry, Chungbuk National University, Chungbuk 28644, Republic of Korea. ³Department of Chemistry, Ulsan National Institute of Science and Technology (UNIST), UNIST-gil 50, Ulsan 44919, Republic of Korea. ✉email: dmj@seas.upenn.edu

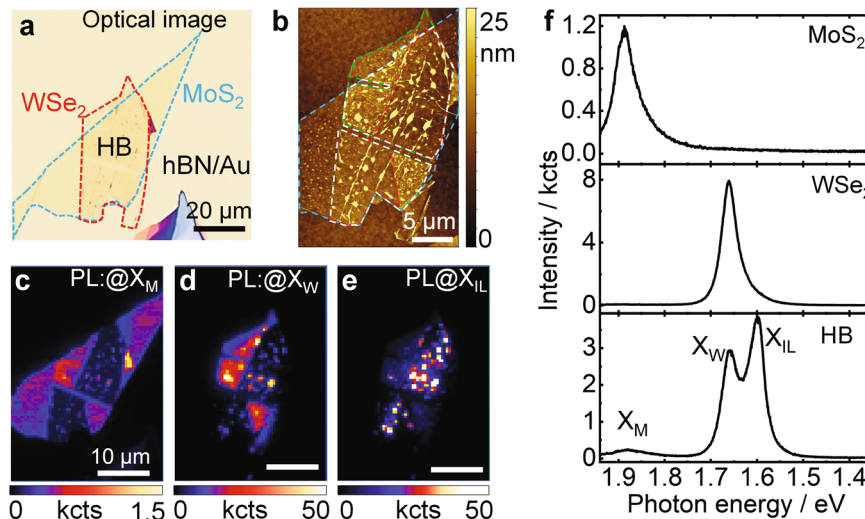


Fig. 1 Far-field optical characterization of HB. **a** Optical image and **(b)** AFM topography of one of the $\text{MoS}_2/\text{WSe}_2$ HB sample prepared on 3 nm hBN/Au substrate. **c–e** PL maps of intralayer exciton MoS_2 (X_M), WSe_2 (X_W) and interlayer exciton (ILX) across $\text{MoS}_2/\text{WSe}_2$ interface respectively. Areas where strong interfacial coupling is established ILX have strong emission followed by quenching of intralayer X_M and X_W . **f** Three representative PL spectra of MoS_2 , WSe_2 , and HB regions displaying characteristic PL spectra of intralayer and interlayer excitons.

(sub-nm cavity) when the junction current flows through the channel. This is particularly relevant since previous works have predicted that tip-induced tunneling through the TMDC monolayers to the metal substrate can reduce the strength of the plasmonic field in the sub-nm cavity and hence decrease the intralayer excitonic emission^{24,25}.

Here, we conduct a systematic investigation into the effect of junction current on the dynamics of intralayer and interlayer exciton-plasmon interactions in TMDC HBs within the quantum plasmonic regime, using a finely tune tip-sample cavity in a TEPL configuration. We utilize $\text{MoS}_2/\text{WSe}_2$ HBs as a test bench on a hBN/Au substrate. Our findings indicate that as the tip-sample distance decreases below 1 nm, in the absence of junction current, intralayer exciton amplifies while ILXs decrease drastically due to the Purcell effect and stronger nonradiative coupling to the plasmon field, respectively. Moreover, once a channel is established for current to flow through the HB/ hBN to the Au substrate, a reverse trend is observed. Using a rate equation model, we qualitatively determined all the coupling parameters, including the dynamics of exciton-plasmon interactions. To the best of our knowledge, our results present the first experimental demonstration of the dynamics of exciton-plasmon interactions in the presence of junction current in the quantum plasmonic regime.

RESULTS AND DISCUSSIONS

Far-field characterizations of the HB

Figure 1a, b show an optical image and atomic force microscope (AFM) topography, respectively, of one of the $\text{MoS}_2/\text{WSe}_2$ HB samples prepared on hBN/Au substrate. Details of the sample preparation can be found in the Method section and Supplementary Note 1. Three far-field PL maps are created: two for intralayer excitons X_M (monolayer MoS_2) and X_W (monolayer WSe_2), and one for interlayer exciton X_{IL} (HB) across the $\text{MoS}_2/\text{WSe}_2$ interface, respectively, and presented in Fig. 1c–e. Three corresponding far-field PL spectra and PL maps, areas marked by the red dashed lines only produce strong ILXs, suggesting better interfacial coupling. We also perform complementary surface potential mapping with/without illumination to further validate our hypothesis. Details of the Kelvin probe force microscope (KPFM) measurements can be found in the Supplementary Note 2. We observe a strong ILX emission followed by heavily quenched intralayer X_M and X_W

emission on the areas marked by red dashed lines, a hallmark of the ILX formation process.

Nano-PL investigation of the HB

After initial far-field characterization, we perform TEPL measurements on areas of strong interfacial coupling. Figure 2a shows a schematic of the TEPL measurements. We use an Au tip for the TEPL measurements under 633 nm excitation. The introduction of an Au substrate creates a plasmonic dimer cavity, the polarization of which is perpendicular to the basal plane of the HB (as shown by **E** in the scheme). We also tune the tip-sample distance (d) via the AFM piezo actuator to investigate exciton dynamics in the HBs. We use 3 nm hBN grown by chemical vapor deposition (CVD) as the insulating barrier between HBs and the substrate. Figure 2b displays an AFM topography image taken across the boundary of HB and WSe_2 . The white dashed line is drawn as a guide to the eye along the border line. A TEPL hyperspectral map is acquired across the boundary and superimposed on the corresponding topography area within the AFM image in Fig. 2b. The TEPL map is created for the X_{IL} spectral range. Two representative TEPL spectra of the two regions (red and blue circles on the TEPL map) are shown in Fig. 2c. The orange rectangular shade is the spectral area for which the X_{IL} map is created in Fig. 2b. As can be seen, TEPL spectra of HB is dominated by ILX emission, with both intralayer X_M and X_W strongly quenched. It should be mentioned that the nanobubbles formed during the sample preparation process have a marked effect on the PL emission from them, even in the region where a strong interfacial coupling between $\text{WSe}_2/\text{MoS}_2$ occurs. A comparative far-field and near-field study of PL emission from the nanobubble and flat HB is presented in the Supplementary Notes 3 and 4, respectively. As shown in Supplementary Fig. 3, the PL response on the nanobubbles is strongly heterogeneous, which may arise due to the variation of the localized strain depending on the size/shape of the nanobubbles²⁶. Nevertheless, the TEPL map shown in Fig. 2b exhibits a spatially homogeneous distribution of the X_{IL} intensity in the flat HB region. Therefore, to maintain consistency and avoid any ambiguity in our analysis, we exclude any detailed study of bubbles in HB regions in the present work. Additionally, since WSe_2 is known for its lowest-lying dark exciton and its higher quantum yield in the near-field geometry at room temperature, we also performed deconvolution of the near-field spectra for clarity of each peak's contribution. Figure 2d presents a

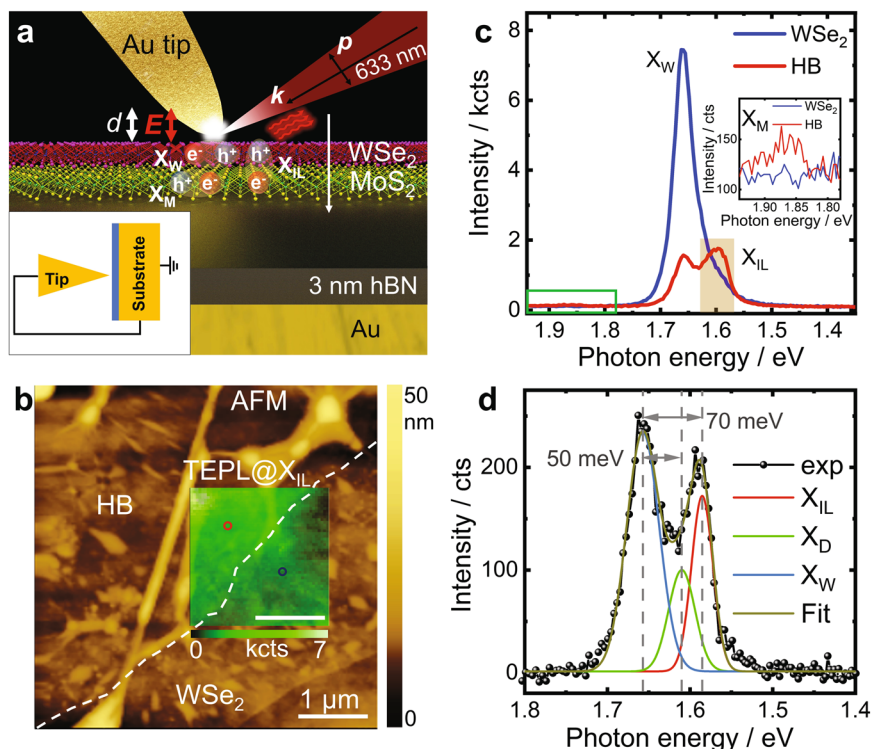


Fig. 2 TEPL study of HB. **a** Schematic illustration of TEPL measurements. In-plane intralayer X_M and X_W and out-of-plane interlayer X_{IL} were excited/amplified by the plasmonic field created at the tip apex under 633 nm excitation. Introduction of a Au substrate created a dimer cavity with the polarization direction perpendicular to the basal plane of the HB. Tip-sample distance was tuned via AFM piezo actuator from a few nm to sub-nm gap and TEPL signal was collected. Inset: the schematic of the electrical configuration of the tip-sample junction. **b** AFM topography image at the boundary of the HB and WSe_2 . Inset: a TEPL map acquired for X_{IL} across the boundary superimposed on the corresponding topography area. **c** Two representative TEPL spectra on the map taken from red and blue circles marked on the TEPL map image. Orange shade on the TEPL spectra is the spectral region for which the TEPL map was created. Inset: zoomed in spectral range covered by the green box highlighting X_M . **d** Deconvoluted TEPL spectra on flat HB using three gaussian peaks.

deconvoluted TEPL spectra of the HB in the spectral range of 1.8–1.3 eV using three gaussian peaks. While the WSe_2 dark exciton lies around 50 meV below the neutral X_W peak, ILX emission (X_{IL}) is red shifted by ~ 70 meV from the X_W and agrees well with the far-field results.

Exciton-cavity dynamics of the HB

In order to investigate sub-nm tip-sample gap dynamics of exciton-plasmon interaction for both intra- and interlayer excitons in HB, we acquire TEPL spectra as a function of tip-sample distance at each point. In addition, we simultaneously record the junction current profile (current flowing from the tip to the substrate through the HB) as a function of tip-sample distances. The current profile is recorded in the short circuit configuration (*i.e.* tip and substrate are electrically connected and the bias voltage, $V = 0$ V as shown in the inset of Fig. 2a). Therefore, the driving force for the current flow in the sub-nm gap (quantum plasmonic regime) can be a combination of the tunneling of tip hot electrons through HB to the Au substrate and the photovoltage created at the HB interface under 633 nm excitation^{27,28}. Important to note that we consistently observe junction current at random points on the HB/hBN/Au sample. As mentioned earlier, we use a CVD-grown 3 nm thick hBN film as the insulating barrier between the HB and Au substrate. During the transfer process of the CVD-grown hBN film onto the Au substrate using the PMMA-assisted wet transfer method from the sapphire substrate (see Method section), it is possible that the quality of the film is compromised, and random channels are opened for the current flow between the tip and substrate. To support our hypothesis, we also perform conductive AFM mapping on hBN/Au areas adjacent to the HB.

Results of the conductive AFM mapping of hBN film are presented in the Supplementary Fig. 5.

Figure 3a, b show two sets of TEPL evolution as a function of tip-sample gap with junction current off and on, respectively. These two data sets are recorded on two different points in the same TEPL map shown in Fig. 2b. As measured tip-sample gap-dependent TEPL spectra for both current off and on conditions shown in Fig. 3a, b are presented in the Supplementary Fig. 6, respectively. The corresponding current vs tip-sample distance graphs are presented in Fig. 3c. Since electrons are flowing from the tip to the substrate, and the substrate is grounded, we observe a negative current as a function of tip-sample distance. For the tip-sample distance-dependent study, we vary the AFM piezo actuator and record the corresponding Force curves, from which the actual tip-sample distances are calculated. Details of the tip-sample distance determination procedure can be found in the Supplementary Note 7.

It should be noted that we have two dimension specific gaps between the tip and the material system: (i) tip-sample gap (varied from the classical regime to the quantum plasmonic regime) and (ii) tip – substrate gap (which is equal to the hBN/HB thickness + tip – sample gap). Hence, for simplicity, we refer to the tip-substrate gap as a cavity, which is discussed in more detail in the analytical model section (Supplementary Note 8). PL evolution without junction current reveals two distinct tip-sample gap regimes: (i) in the nm gap (>1 nm) regime, all exciton intensities are increasing, and (ii) in the sub-nm gap regime intralayer (interlayer) exciton intensity is increasing (decreasing). Moreover, we can also observe that in the sub-nm gap X_M intensity gradually decreases with gap size (see Supplementary

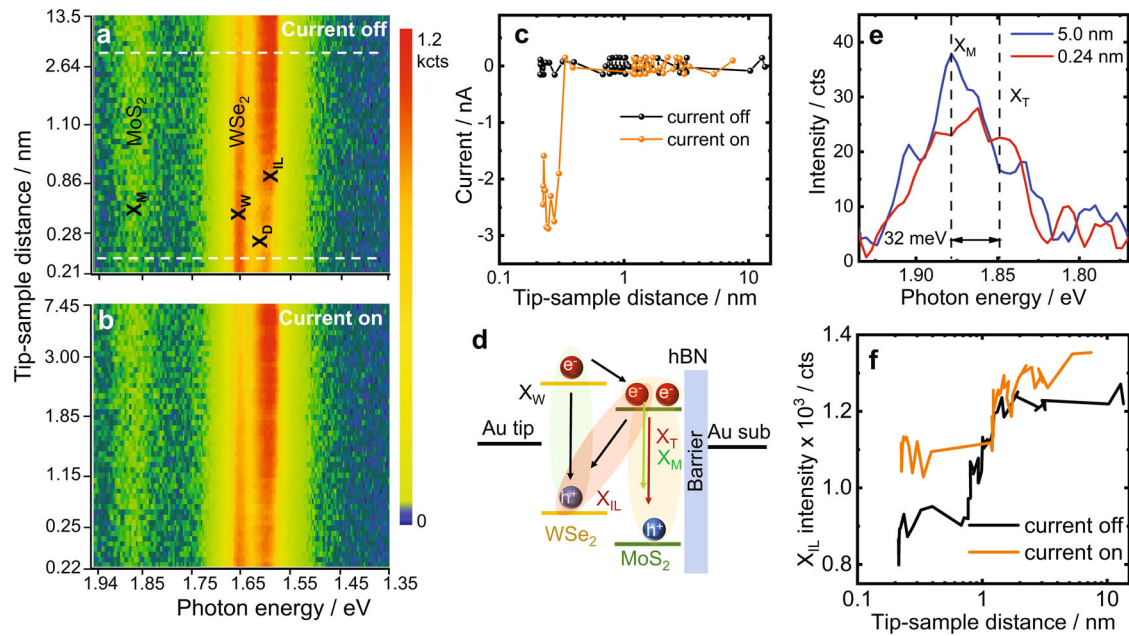


Fig. 3 Exciton tuning in the quantum tunnelling regime. Spectral evolution of TEPL signal as a function of tip-sample distance (a) when no current flows through the HB and (b) when current flows through the HB. (c) Junction current profile as a function of tip-sample distance for the case of (a) and (b). Electrical configuration of the tip-sample junction is shown in Fig. 2a. Current was measured simultaneously in the short circuit configuration ($V = 0$ V). **d** Schematic of the HB band alignment showing trion formation in MoS₂ when the tip is in the sub-nm gap. **e** Comparison of MoS₂ TEPL spectra at two different tip-sample distances (white dashed lines in (a)) for the case of no junction current. In addition to the X_M , we could also observe trion, X_T in MoS₂. **f** X_{IL} evolution as a function of tip-sample distance for the two cases (current off and on).

Fig. 6c). Additionally, the contribution from dark exciton (X_D) of WSe₂ becomes apparent as the gap shrinks. Observation of dark excitons in WSe₂ in the TEPL configuration is a well-known phenomenon, which originates from the radiative exchange between the exciton dipole and the tip plasmon^{29,30}. However, the decreasing trend of X_M may lie in the exciton population and interfacial charge transfer process, as the tip-sample gap shrinks. A schematic illustration of the exciton population and relaxation process in the HB in the tip-sample gap is shown in Fig. 3d. Excitons are populated in both monolayers by gap plasmon excitation. Ultrafast interfacial charge transfer allows electrons in WSe₂ to cross the interface and jump to the conduction band of MoS₂. Since hBN acts as the barrier for electrons to move to the Au substrate, overall electron concentration may increase momentarily in MoS₂. This results in the radiative relaxation of ILX across the interface and the formation of trion in MoS₂. Hence, we observe a gradual decrease in X_M intensity as the gap shrinks. Figure 3e displays two TEPL spectra in the MoS₂ spectral regime taken along the white dashed lines in Fig. 3a. As it is seen, PL spectra at 0.23 nm tip-sample distance clearly shows an overall broad spectrum with a trion peak at 35 meV¹ below the main excitonic peak in MoS₂, and supports our hypothesis.

An interesting phenomenon is observed when the junction current flowed (Fig. 3b) between the tip and the sample, especially in the sub-nm gap (quantum plasmonic regime). Both the intralayer exciton Purcell enhancement and ILX showing a decreasing trend are slowed down as the current started flowing in the shrinking gap. The evolution of ILX intensity as a function of gap size for both current off and on is shown in Fig. 3f for comparison. PL enhancement in the tip-sample cavity (tip-sample gap plus the HB/hBN thickness) involves a competition between the Purcell effect and the tip-induced nonradiative quenching¹⁸. Both the Purcell enhancement and the tip-induced nonradiative damping are scaled to a power law of the cavity size. Especially, nonradiative relaxation becomes significant in the sub-nm tip-sample gap via dipole coupling to the tip-sample cavity plasmon

due to the ultrafast ohmic Drude loss³¹. Therefore, in the sub-nm gap, we observed a sharp rise of X_W emission due to the Purcell effect and ILX quenching since tip-induced nonradiative damping of intralayer excitons becomes faster than the interlayer charge transfer. However, as soon as the current starts flowing between the tip and the sample, the strength of the cavity plasmon weakens. This results in reduced Purcell enhancement and slower nonradiative damping of intralayer excitons, resulting in the boosting of ILX emission in the sub-nm gap. To the best of our knowledge, our results are the first experimental demonstration of exciton-plasmon coupling in the presence of junction current recorded in a near-field spectroscopy experiment.

Rate-equation model for exciton-cavity dynamics

To understand the tip-sample gap-induced contribution of radiative and nonradiative damping as well as the near-field enhancement, we fit the PL evolutions using a steady state rate equation model described in the previous work²¹. Details of our model and fitting procedure are discussed in the Supplementary Note 8. Evolution of all excitonic populations is the product of various excitation and relaxation rates inside the cavity. The cavity-induced field enhancement (excitation) can be scaled as $F \propto (R/z)^m$, with R being the tip radius, z being the distance between the tip and Au substrate, and m is the geometrical factor. In contrast, the population of ILX depends on the interlayer charge transfer upon the intralayer exciton population. We divide the model into two regions: one for the nm gap and the other for the sub-nm gap, with the only adjusting parameter is the scaling factor. The total decay rate of each excitonic species is the sum of three terms: (i) cavity-controlled (Purcell effect) radiative decay scaled as $\Gamma^{\text{rad}} \propto (z+d)^{-n} + \Gamma_0^{\text{rad}}$, with d is the minimum tip-sample distance, n is the scaling factor, and Γ_0^{rad} is the free space radiative decay; (ii) cavity-induced nonradiative recombination described by $\Gamma^{\text{nr}} \propto (R/(z+d))^l$, with l being the scaling factor; and (iii) first-order intrinsic nonradiative relaxation rate Γ_0^{nr} . The

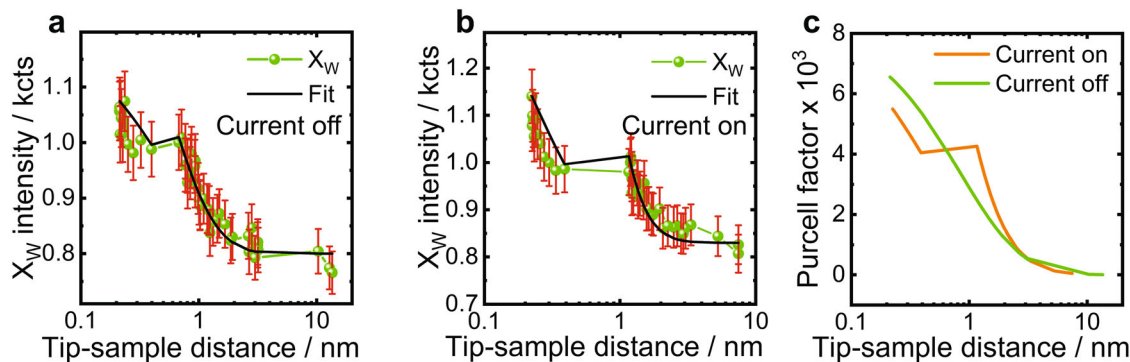


Fig. 4 Rate equation fit to the PL evolution. PL evolution of intralayer X_W together with fitted curve as a function of tip-sample gap for (a) no current in the junction and (b) current flowing in the junction. The error bar presented in (a) and (b) are the fit errors of the integrated intensity using a gaussian peak. c Calculated Purcell factor in the tip-sample cavity with/without junction current.

value of $\Gamma_0 = 2\hbar/\tau_0$, with τ_0^{rad} and τ_0^{nrad} are assumed to be 0.7 ns and 1.5 ps, respectively (taken from refs. 21,32). Using these assumptions in the steady-state limit of exciton population, we fit the PL evolution of X_W for both sets of results shown in Fig. 3a, b. We are not able to extract the X_M intensity profile reliably due to its very low quantum yield. Therefore, we do not fit tip-substrate cavity-dependent X_M evolution in the present study. Moreover, since the ILX population requires contribution from both X_M and X_W , we need fit parameters from both intralayer excitonic species for a reliable fitting. Hence, we also avoid any qualitative analytical discussion on ILX parameters as well. Figure 4a, b present fitted X_W evolution as a function of tip-sample distance for the PL evolution graphs shown in Fig. 3a, b, respectively. The PL evolution reveals two distinct distance-dependent regimes, which our model fits well. Since the model requires analytical expression of both radiative and nonradiative relaxation rates, it is possible to extract radiative and nonradiative lifetimes of fitted excitons in the varying tip-sample cavity. A qualitative discussion on radiative and nonradiative relaxation of X_W in the tip-sample cavity is presented in the Supplementary Note 8 and Supplementary Fig. 8. Here, the evolution of the Purcell factor in the tip-substrate cavity is going to be discussed. Figure 4c shows the evolution of the Purcell factor in the tip-substrate cavity extracted from the fitting presented in Fig. 4a, b respectively. Our model provided a similar scaling exponent to the model described in ref. 21. for the Purcell enhancement in the absence of junction current (see Supplementary Table 1). However, a more dramatic change can be seen in the case of the current on. The cavity-dependent field enhancement initially increases at a scaling exponent of 5.6. However, as soon as the current starts flowing field strength is suppressed by an exponential factor of 0.5. The maximum Purcell factor is extracted to be $F \approx 6 \times 10^3$ calculated for the case of current off is consistent with previous TEPL measurements^{33–35}. Additionally, the exponent factor $m \approx 5$ indicates that our near-field geometry is more like a point dipole on a plane for which the Purcell factor is expected to grow as $1/z^6$ ³⁶. This is most likely due to the fact that 3 nm hBN film on top of Au substrate results in reduced coupling between the tip and the Au substrate.

In summary, this work reports on tailoring exciton dynamics in the near-field from the classical plasmonic regime (few nm) to quantum plasmonic regime (sub-nm) with/without junction current in TMDC HBs using an Au tip + Au substrate-induced plasmonic cavity. We show that in the absence of a junction current intralayer and interlayer exciton show an opposite trend as a function of gap size in the sub-nm cavity. We explain this behavior by two competing phenomena. While the cavity field amplifies intralayer excitons dramatically in the quantum plasmonic regime, it also enhances nonradiative damping via coupling between exciton dipole and tip plasmon for which interlayer exciton suffers the most. In contrast, when current flows in the

junction, it quenches the Purcell factor of the sub-nm cavity dramatically, and at the same time boosts ILX by reducing the nonradiative relaxation of excitons. Our work provides a solid understanding of exciton dynamics in the quantum plasmonic regime with/without junction current and demonstrates a clear pathway of boosting exciton densities to enable new optoelectronic applications, and to induced room temperature exciton condensates via tuning plasmonic cavity in the quantum tunneling regime.

METHODS

Sample preparation

MoS₂/WSe₂ HBs were prepared using PDMS assisted deterministic dry transfer method. Since interface contamination is one of the major challenges for the ILXs formation, we used PDMS to PDMS pick up/creation of HBs. Details of the HBs creation are schematically presented in the Supplementary Fig. 1. HBs prepared in this way show strong ILX emission as shown in Fig. 1. We used CVD-grown 3 nm thick hBN film on top of a 100 nm thick Au film as the substrate. The 3 nm thick hBN film was prepared by a low-pressure CVD system on a c-plane sapphire substrate using ammonia borane as a precursor. The details of the CVD procedure of hBN and PMMA-assisted wet transfer of hBN on arbitrary substrates can be found in the literature³⁷. After the preparation of the individual HBs, the bilayer stacks were then transferred onto hBN/Au substrate.

Far-field characterization

Far-field optical measurements were conducted using a Horiba LabRam HR evolution confocal microscope coupled with an electron multiplying charged couple detector dispersed by a 100 l/gr grating. A 633 nm solid-state laser was used for the excitation with laser power of 17 μ W focused onto the sample surface via 100 \times 0.9 NA objective.

Nano-PL investigation

TEPL measurements were performed using a Horiba NanoRaman platform in the side illumination/collection configurations, which consists of an atomic force microscope from AIST-NT and a LabRam Evolution spectrometer. The Au tips used in the experiments were purchased from Horiba and suited for near-field measurements under 633 nm excitation. The laser power was kept at 17 μ W and focused onto the tip via a 100 \times 0.7 NA long working distance objective. The exposure time was 0.2 s. TEPL hyperspectral maps were acquired in the spectop mode (a contact/noncontact hybrid mode developed by Horiba), in which half of the time ($t/2$) the tip is in contact with the sample to acquire

the near-field signal and the rest half of the time (t_2) the tip is operating in the intermittent contact mode to acquire the far-field signal and the AFM topography on each pixel with the total time defined by $t = t_1 + t_2$ and $t_1 = t_2 =$ exposure time.

Force spectroscopy and exciton-cavity dynamics

For tip-sample distance-dependent TEPL measurements, a varying DC voltage was applied gradually to the piezo-actuator connected to the sample stage for fine-tuning of the tip-sample cavity from few nm to sub-nm. A total of 50 data points were collected for a large piezo-actuator displacement (150 nm–200 nm). At each point, a TEPL spectra was acquired using an exposure time of 0.2 s. In addition to the TEPL spectra, force vs distance curves and junction current were also monitored for the mentioned piezo-actuator tuning range for each experimental data set. The actual tip-sample distance, d was calculated from the acquired force vs distance curve. Details of the calculation can be found in the Supplementary Note 7.

KPFM measurements

KPFM measurements were performed using AFM from AIST-NT and commercially available Cr/Au probes with/without illumination under 633 nm excitation.

DATA AVAILABILITY

The data that support the findings of this study are available on request from the corresponding author.

Received: 1 June 2023; Accepted: 31 August 2023;

Published online: 11 September 2023

REFERENCES

- Kylänpää, I. & Komsa, H. P. Binding energies of exciton complexes in transition metal dichalcogenide monolayers and effect of dielectric environment. *Phys. Rev. B - Condens. Matter Mater. Phys.* **92**, 1–6 (2015).
- Jin, C. et al. Ultrafast dynamics in van der Waals heterostructures. *Nat. Nanotechnol.* **13**, 994–1003 (2018).
- Liu, Y. et al. Van der Waals heterostructures and devices. *Nat. Rev. Mater.* **1**, 16042 (2016).
- Ross, J. S. et al. Interlayer exciton optoelectronics in a 2D heterostructure p-n junction. *Nano Lett.* **17**, 638–643 (2017).
- Combescot, M., Combescot, R. & Dubin, F. Bose-Einstein condensation and indirect excitons: A review. *Rep. Prog. Phys.* **80**, 066501 (2017).
- Jiang, C. et al. Microsecond dark-exciton valley polarization memory in two-dimensional heterostructures. *Nat. Commun.* **9**, 753 (2018).
- Paik, E. Y. et al. Interlayer exciton laser of extended spatial coherence in atomically thin heterostructures. *Nat.* **576**, 80–84 (2019).
- Jiang, Y., Chen, S., Zheng, W., Zheng, B. & Pan, A. Interlayer exciton formation, relaxation, and transport in TMD van der Waals heterostructures. *Light Sci. Appl.* **10**, 1–29 (2021).
- Lin, K.-Q. A roadmap for interlayer excitons. *Light Sci. Appl.* **10**, 99 (2021).
- Palacios-Berraquero, C. et al. Large-scale quantum-emitter arrays in atomically thin semiconductors. *Nat. Commun.* **8**, 1–6 (2017).
- Raja, A. et al. Coulomb engineering of the bandgap and excitons in two-dimensional materials. *Nat. Commun.* **8**, 1–7 (2017).
- Wang, G. et al. Colloquium: Excitons in atomically thin transition metal dichalcogenides. *Rev. Mod. Phys.* **90**, 021001 (2018).
- Seyler, K. L. et al. Signatures of moiré-trapped valley excitons in MoSe₂/WSe₂ heterobilayers. *Nature* **567**, 66–70 (2019).
- Sternbach, A. J. et al. Programmable hyperbolic polaritons in van der Waals semiconductors. *Science (80-)* **371**, 617–620 (2021).
- Schneider, C., Glazov, M. M., Korn, T., Höfling, S. & Urbaszek, B. Two-dimensional semiconductors in the regime of strong light-matter coupling. *Nat. Commun.* **2018 91 9**, 1–9 (2018).
- As'Ham, K., Al-Ani, I., Huang, L., Miroshnichenko, A. E. & Hattori, H. T. Boosting strong coupling in a hybrid WSe₂Monolayer-Anapole-Plasmon system. *ACS Photonics* **8**, 489–496 (2021).
- Al-Ani, I. A. M. et al. Recent advances on strong light-matter coupling in atomically thin TMDC semiconductor materials. *J. Opt.* **24**, 053001 (2022).
- Moroz, A. Non-radiative decay of a dipole emitter close to a metallic nanoparticle: Importance of higher-order multipole contributions. *Opt. Commun.* **283**, 2277–2287 (2010).
- Rivera, P. et al. Coupling of photonic crystal cavity and interlayer exciton in heterobilayer of transition metal dichalcogenides. *2D Mater.* **7**, 015027 (2019).
- Förg, M. et al. Cavity-control of interlayer excitons in van der Waals heterostructures. *Nat. Commun.* **10**, 3697 (2019).
- May, M. A. et al. Nanocavity clock spectroscopy: resolving competing exciton dynamics in WSe₂/MoSe₂Heterobilayers. *Nano Lett.* **21**, 522–528 (2021).
- Rivera, P. et al. Observation of long-lived interlayer excitons in monolayer MoSe₂-WSe₂ heterostructures. *Nat. Commun.* **6**, 1–6 (2015).
- Nagler, P. et al. Interlayer exciton dynamics in a dichalcogenide monolayer heterostructure. *2D Mater.* **4**, 0–9 (2017).
- He, Z. et al. Quantum plasmonic control of trions in a picocavity with monolayer WS₂. *Sci. Adv.* **5**, eaau8763 (2019).
- Ferrera, M. et al. Controlling excitons in the quantum tunneling regime in a hybrid plasmonic/2D semiconductor interface. *Appl. Phys. Rev.* **9**, 031401 (2022).
- Darlington, T. P. et al. Imaging strain-localized excitons in nanoscale bubbles of monolayer WSe₂ at room temperature. *Nat. Nanotechnol.* **15**, 854–860 (2020).
- Savage, K. J. et al. Revealing the quantum regime in tunnelling plasmonics. *Nature* **491**, 574–577 (2012).
- Rahaman, M. et al. Probing interlayer excitons in a vertical van der Waals p-n junction using a scanning probe microscopy technique. *J. Phys. Condens. Matter* **31**, 114001 (2019).
- Park, K. D., Jiang, T., Clark, G., Xu, X. & Raschke, M. B. Radiative control of dark excitons at room temperature by nano-optical antenna-tip Purcell effect. *Nat. Nanotechnol.* **13**, 59–64 (2018).
- Rahaman, M. et al. Observation of Room-Temperature Dark Exciton Emission in Nanopatch-Decorated Monolayer WSe₂ on Metal Substrate. *Adv. Opt. Mater.* **9**, 2101801 (2021).
- Förster, T. Zwischenmolekulare Energiewanderung und Fluoreszenz. *Ann. Phys.* **437**, 55–75 (1948).
- Palummo, M., Bernardi, M. & Grossman, J. C. Exciton radiative lifetimes in two-dimensional transition metal dichalcogenides. *Nano Lett.* **15**, 2794–2800 (2015).
- Suh, J. Y. et al. Plasmonic bowtie nanolaser arrays. *Nano Lett.* **12**, 5769–5774 (2012).
- Wei, W., Yan, X. & Zhang, X. Ultrahigh Purcell factor in low-threshold nanolaser based on asymmetric hybrid plasmonic cavity. *Sci. Rep.* **6**, 1–7 (2016).
- Park, K. D. & Raschke, M. B. Polarization Control with Plasmonic Antenna Tips: A Universal Approach to Optical Nanocrystallography and Vector-Field Imaging. *Nano Lett.* **18**, 2912–2917 (2018).
- Behr, N. & Raschke, M. B. Optical antenna properties of scanning probe tips: Plasmonic light scattering, tip-sample coupling, and near-field enhancement. *J. Phys. Chem. C* **112**, 3766–3773 (2008).
- Jang, A. R. et al. Wafer-Scale and Wrinkle-Free Epitaxial Growth of Single-Orientated Multilayer Hexagonal Boron Nitride on Sapphire. *Nano Lett.* **16**, 3360–3366 (2016).

ACKNOWLEDGEMENTS

M.R. acknowledges support from Deutsche Forschungsgemeinschaft (DFG, German Research Foundation) for Walter Benjamin Fellowship (award no. RA 3646/1-1). D.J. and G. Kim acknowledge primary support for this work by the Asian Office of Aerospace Research and Development (AOARD) of the Air Force Office of Scientific Research (AFOSR) FA2386-20-1-4074. The sample fabrication, assembly and characterization were carried out at the Singh Center for Nanotechnology at the University of Pennsylvania which is supported by the National Science Foundation (NSF) National Nanotechnology Coordinated Infrastructure Program grant NNCI-1542153. K.Y.M. and H.S.S. acknowledge the support from the National Research Foundation, Republic of Korea via the research fund (NRF-2021R1A3B1077184). S.S. acknowledges support from Basic Science Research Program through the National Research Foundation of Korea (NRF) funded by the Ministry of Education (Grant number 2021R1A6A3A14038492).

AUTHOR CONTRIBUTIONS

M.R. and D.J. conceived the idea and designed the research. M.R. implemented the project via performing the experiments and simulations with the help of G.K. and S.S. G.K. assisted in sample preparation. K.Y.M. and H.S.S. prepared the hBN film. M.R. and D.J. wrote the manuscript; all the authors revised and commented on the manuscript. All authors contributed to the writing of manuscript and interpretation of the data.

COMPETING INTERESTS

The authors declare no competing interests.

ADDITIONAL INFORMATION

Supplementary information The online version contains supplementary material available at <https://doi.org/10.1038/s41699-023-00428-7>.

Correspondence and requests for materials should be addressed to Deep Jariwala.

Reprints and permission information is available at <http://www.nature.com/reprints>

Publisher's note Springer Nature remains neutral with regard to jurisdictional claims in published maps and institutional affiliations.



Open Access This article is licensed under a Creative Commons Attribution 4.0 International License, which permits use, sharing, adaptation, distribution and reproduction in any medium or format, as long as you give appropriate credit to the original author(s) and the source, provide a link to the Creative Commons license, and indicate if changes were made. The images or other third party material in this article are included in the article's Creative Commons license, unless indicated otherwise in a credit line to the material. If material is not included in the article's Creative Commons license and your intended use is not permitted by statutory regulation or exceeds the permitted use, you will need to obtain permission directly from the copyright holder. To view a copy of this license, visit <http://creativecommons.org/licenses/by/4.0/>.

© The Author(s) 2023